

Selective Laser Sintering versus Multi Jet Fusion: A Comprehensive Comparison Study Based on the Properties of Glass Beads-Reinforced Polyamide 12

*Original*

Selective Laser Sintering versus Multi Jet Fusion: A Comprehensive Comparison Study Based on the Properties of Glass Beads-Reinforced Polyamide 12 / Lupone, F.; Padovano, E.; Lambertini, V. G.; Sampieri, R.; Casamento, F.; Zecchi, S.; Badini, C.. - In: ADVANCED ENGINEERING MATERIALS. - ISSN 1527-2648. - 26:3(2024).  
[10.1002/adem.202301345]

*Availability:*

This version is available at: 11583/2984948 since: 2024-01-10T14:43:24Z

*Publisher:*

Wiley-VCH

*Published*

DOI:10.1002/adem.202301345

*Terms of use:*

This article is made available under terms and conditions as specified in the corresponding bibliographic description in the repository

*Publisher copyright*

(Article begins on next page)

# Selective Laser Sintering versus Multi Jet Fusion: A Comprehensive Comparison Study Based on the Properties of Glass Beads-Reinforced Polyamide 12

Federico Lupone, Elisa Padovano,\* Vito Guido Lambertini, Roberta Sampieri, Francesco Casamento, Silvia Zecchi, and Claudio Badini

Selective laser sintering (SLS) and multi jet fusion (MJF) are the most widespread powder bed fusion additive manufacturing techniques for fabricating polymeric parts since they offer great design flexibility, productivity, and geometrical accuracy. However, these technologies differ in the thermal energy source used to melt the powders as well as the innovative use of printing agents featured in the latter one to promote material consolidation and to avoid thermal bleeding at the part contours. The use of a single powder made of glass beads-reinforced polyamide 12 (PA12/GB) for the fabrication of MJF and SLS samples makes possible a systematic comparison of the printed parts properties. A thoughtful analysis of the microstructure and mechanical properties of the samples reveals differences and peculiarities between the two technologies. SLS exhibits lower porosity and higher mechanical performances when the parts are printed along the build plane thanks to the powerful heating ensured by the laser. In contrast, MJF samples show higher mechanical isotropy with great flexural and tensile behavior for vertically oriented parts. The role of glass beads in the material behavior is defined by their mechanical properties, meaning higher rigidity and lower strength compared to neat PA12, and fracture mechanism.

## 1. Introduction

Powder bed fusion (PBF) technologies are a subfamily of additive manufacturing (AM) techniques which involve the subsequent deposition of raw material in powder form and the use of an energy source to melt the particles in selected areas of the powder bed.<sup>[1]</sup> By varying the type of heat source and the material it interacts with, different PBF printing techniques can be distinguished.<sup>[2]</sup> Selective laser sintering (SLS) and multi jet fusion (MJF) are the most employed techniques for the processing of polymeric components.<sup>[2]</sup>

As confirmed from the worldwide sales data published in the 2022 Wohlers report, the polymer powders market has grown by 43% in the last year, thus surpassing photopolymer resins as the most adopted AM material.<sup>[3]</sup> This underlines the significant impact that polymer AM has at industrial scale. All polymer PBF techniques can be


described in three main steps.<sup>[4]</sup> First, the build plate is gradually preheated at a temperature just below the melting onset of the polymer and the starting powder is homogeneously spread to form a thin layer with fixed thickness. Then, a heat source induces the melting of the particles in selected area of the powder bed according to a computer-aided design (CAD) model. The consolidation of the layer and its bonding with the previous one take place thanks to the coalescence and successive solidification of the powders. Once each layer is scanned, the build plate is dropped by a layer height and these steps are repeated until the fabrication of the 3D part is completed.<sup>[4]</sup>

In the context of polymer PBF technologies, SLS was the first commercialized process, developed in the late 1980s at the University of Texas,<sup>[1]</sup> and nowadays is one of the most widespread AM methods for the processing of polymer-based materials. In addition to the main advantages typical of AM techniques such as the possibility to manufacture fully customized parts with complex geometrical shape without the need of molds and tools, and avoiding the production of scraps, the high dimensional accuracy and good properties of SLS parts as well as a growing choice of available materials make this technology attractive at industrial scale, mainly for aerospace, automotive, medical, or tooling applications.<sup>[5,6]</sup> Moreover, owing to the preheating step,

F. Lupone, E. Padovano, F. Casamento, S. Zecchi, C. Badini  
Department of Applied Science and Technology  
Politecnico di Torino  
Corso Duca degli Abruzzi 24, 10129 Torino, Italy  
E-mail: elisa.padovano@polito.it

V. G. Lambertini  
Centro Ricerche Fiat  
Stellantis  
Strada Torino 50, 10043 Orbassano, Italy

R. Sampieri  
Stellantis  
Prototype & Pilot Operation  
Via Biscaretti di Ruffia 90/A, 10135 Torino, Italy

 The ORCID identification number(s) for the author(s) of this article can be found under <https://doi.org/10.1002/adem.202301345>.

© 2023 The Authors. Advanced Engineering Materials published by Wiley-VCH GmbH. This is an open access article under the terms of the Creative Commons Attribution-NonCommercial-NoDerivs License, which permits use and distribution in any medium, provided the original work is properly cited, the use is non-commercial and no modifications or adaptations are made.

DOI: 10.1002/adem.202301345

SLS does not require support structures for part fabrication, also for overhanging features or thin walls. This allows to increase in the saturation of the build chamber space, thus enabling the high-volume production of polymeric parts.<sup>[6]</sup>

As an alternative, the last decade saw the birth and development of MJF technology. Patented in 2014 and put into the market in 2016 by Hewlett-Packard Inc. (HP), MJF works with the same principles of SLS, but it greatly differs for the heat source employed and the material consolidation mechanism.<sup>[1]</sup> In fact, SLS uses a laser beam to selectively fuse the powder particles; this coherent energy source is deflected and focused by galvanometric mirrors and lenses on the powder layer to scan each cross section of the object.<sup>[6]</sup> A CO<sub>2</sub> laser is generally used because the absorption of polymeric materials at the corresponding wavelength of 10.6  $\mu\text{m}$  is high.<sup>[1]</sup> On the contrary, MJF technique involves the use of an array of infrared (IR) lamps, which moves across the powder layer previously impregnated with printing agents on a voxel level (i.e., voxel stands for “volume element”, a 3D analog of the pixel).<sup>[7]</sup> In fact, a series of inkjet heads deposit a fusing agent on selected regions of the powder layer corresponding to the cross-section of the part, and a detailing agent across its perimeter.<sup>[7]</sup> The interaction of the infrared radiation with the impregnated powders promotes the consolidation of the material due to the specific role of the deposited agents. The fusing agent is a radiation-absorbing ink that comprises an aqueous solvent, carbon black, and other organic additives. The carbon black works as an IR-absorbing compound that converts the incoming radiation into thermal energy, thus causing the powders to melt.<sup>[8,9]</sup> The detailing agent serves to inhibit the fusion of the powders surrounding the part by providing a local cooling effect based on solvent evaporation and to improve printing resolution and accuracy.<sup>[8,9]</sup>

Therefore, while in the MJF process, the IR lamps supply a planar energy input to the whole build plate, causing the melting of selected regions of the powder bed where the fusing agents are applied, the SLS laser scans the area of interest line-by-line.<sup>[10]</sup> This has inevitable drawbacks because the build rate is limited to 1200  $\text{cm}^3 \text{h}^{-1}$  for a maximum laser scan speed of 5  $\text{m s}^{-1}$ .<sup>[10,11]</sup> and the fabrication time greatly depends on the size of the cross section of the printed parts.<sup>[12]</sup> By contrast, in MJF, the rapid movement across the build plane of the carriage unit, where the IR lamps and the inkjet heads are located, and the uniform melting of the powders allows a geometry-independent layer processing time of about 10 s.<sup>[10]</sup> This greatly reduces the processing duration with respect to the time-consuming laser scanning method typical of the SLS technique since the build rate could reach value as high as 5058  $\text{cm}^3 \text{h}^{-1}$ .<sup>[13]</sup> Therefore, MJF represents a promising alternative for the processing of powdered polymer systems. However, a direct comparison of SLS and MJF technologies is necessary to evaluate the differences in performances between the respective parts and to decide which process is more suited for certain requirements. In fact, apart from the distinct heat source and consolidation mechanism, also the recoating strategies (i.e., blade vs roller) and powder bed temperature differ between the two PBF techniques.<sup>[12]</sup>

Among the quite limited range of materials available to be processed by SLS, polyamide 12 (PA12), a thermoplastic polymer with a semicrystalline structure, is surely the most used and investigated one.<sup>[5,6]</sup> The use of an energy source such as a

CO<sub>2</sub> laser or an IR lamp causes the melting of the crystalline portion; the low melt viscosity leads to a high coalescence rate and a high densification of the material.<sup>[5,6]</sup> Most research works on MJF were also focused on neat PA12 and different aspects such as mechanical properties,<sup>[14–18]</sup> surface quality,<sup>[10,12,19]</sup> powder aging,<sup>[20]</sup> role of the inks,<sup>[21,22]</sup> and cooling rates<sup>[23,24]</sup> were studied. Therefore, to compare the performances of the parts obtained by SLS and MJF technologies, PA12 has been selected as a reference. Sillani et al.<sup>[12]</sup> deeply investigated the properties of both feedstock and final components produced by these two technologies. With this purpose, two commercially available PA12 powders specifically provided for SLS and MJF, respectively, were used and compared. Powder properties such as particle size and shape distribution, thermal transitions, and phase constitution were found to be similar for the two powdered systems; differences in the fraction of fine particle as well as in the recyclability of the powders (due to end-capping of the polymer chains in MJF feedstock) were however observed.<sup>[12]</sup> Regarding the printed parts, anisotropy was reported when changing the printing orientation from the build plane (i.e., XY) to the Z axis. The similarities and differences between SLS and MJF techniques in terms of raw powders and final parts properties were also evidenced by other authors.<sup>[10,25–27]</sup> Xu et al.<sup>[10]</sup> suggested that the higher heating capability of the laser source compared to the IR lamps induces a higher melting efficiency in SLS, leading to lower pore content and superior stiffness and strength for parts fabricated in the build plane (i.e., XY).<sup>[10]</sup> Rosso et al.<sup>[25]</sup> found that the elongation at break of MJF samples is significantly higher with respect to the SLS counterparts. Cai et al.<sup>[26]</sup> confirmed that both techniques create anisotropic parts as a function of the printing orientation, with the SLS process more susceptible to this effect. Among the three major axes, the highest variation of mechanical properties was recorded in the Z orientation, wherein the tensile strength of MJF samples is 25% higher.<sup>[26]</sup> Calignano et al.<sup>[27]</sup> attributed this large difference to the effect of the fusing agent, which leads to lower volume and number of elongated pores for MJF parts.

However, most of the literature starts from two different powders to fabricate samples by SLS and MJF, respectively, and then compares their final properties.<sup>[10,12,25–28]</sup> By contrast, this work provides a rigorous comparison between the two different technologies since the samples were fabricated by using the same powder, a PA12 reinforced with glass beads, nominally designed for MJF and directly supplied by HP. The samples were then characterized with an equal set of experimental analyses. This approach allows us to clearly distinguish the effect of the different processing conditions and consolidation mechanisms occurring in SLS and MJF on the part performances. Since the literature review suggested that the variation of mechanical properties with part orientation is a critical factor for the potential applications of each technique, this aspect will be the focal point of this study. Moreover, the addition of a glass-based reinforcement to PA12 powders allows us to investigate the effect of these AM techniques on the processing of polymer composites. This represents a novelty since only a couple of research works<sup>[29,30]</sup> are focused on glass beads-reinforced PA12 composites parts manufactured using MJF and these studies lack a direct comparison between their microstructure and mechanical properties and those of the SLS counterparts.

## 2. Experimental Section

### 2.1. Material and Printing Equipment

PA12 powders reinforced with 40 wt% glass beads (PA12/GB) were purchased from Hewlett-Packard (Palo Alto, CA, USA) under the trade name HP 3D High Reusability PA 12 GB. The powders were processed using both MJF and SLS technologies to compare the microstructural and mechanical properties derived from the two different PBF processes. HP Jet Fusion Series 5200 (Hewlett-Packard, Palo Alto, CA, USA) and Sharebot SnowWhite<sup>2</sup> machine (Sharebot S.r.l., Nibionno, Italy) were used for MJF and SLS processing, respectively.

HP Jet Fusion Series 5200 printer is composed of a build unit where the powders are spread by a roller to form a thin layer of fixed thickness and a movable carriage unit containing an array of dual-agent printheads and two sets of fusing IR lamps on both sides.<sup>[7]</sup> The carriage unit moves across the build platform, preheated at a fixed temperature by an overhead IR lamp placed over the print bed, to selectively apply the proprietary fusing and detailing agents in the interior and outside the boundaries of the part, respectively. These agents are dispensed from an array of thermal inkjet nozzles in a discrete manner with high spatial resolution.<sup>[8]</sup> The IR lamps cause the selective melting of the powders in the regions where the fusing agent has been applied, while the detailing ink avoids heat transfer outside the molten area by evaporation.<sup>[7,8]</sup> The build plate is then moved downward by a distance equal to the layer thickness to enable the spreading of a new powder layer by the roller. These steps are iteratively repeated until part completion.<sup>[7,8]</sup> A schematic of the MJF process just described is sketched in Figure 1a.

Sharebot SnowWhite<sup>2</sup> printer uses a 200  $\mu\text{m}$  diameter continuous wave CO<sub>2</sub> laser ( $\lambda = 10.6 \mu\text{m}$ ) to selectively fuse the polymeric powders deposited in subsequent thin layers by a translational recoating blade over the build plate (Figure 1b). The powders are preheated by four halogen lamps placed over the build plate for the entire building process. During the fabrication of each layer, the laser scans the perimeters of the objects before hatching the interior regions.<sup>[31]</sup>

The process parameters for SLS parts were optimized with the aim of minimizing porosity content and avoiding part distortion. The powder bed temperature was set at 171 °C because lower values cause build failure due to part curling. Laser power ( $P$ ), scan speed ( $v$ ), and scan spacing ( $s$ ) were set at 6.3 W, 2400 mm s<sup>-1</sup>, and 100  $\mu\text{m}$ , respectively. Layer height ( $h$ ) was also set at 100  $\mu\text{m}$ . The volumetric laser energy density ( $ED$ ),<sup>[1]</sup> equal to 0.263 J mm<sup>-3</sup> for the optimized sets of parameters, was calculated according to Equation (1):

$$ED = \frac{P}{vsh} \quad (1)$$

In the case of MJF technique, the only print mode available to process 3D High Reusability PA12 GB powders, consisting of two printing passes spending about 10 s per layer, was adopted.<sup>[29,30,32]</sup> However, details about the process parameters (e.g., lamps irradiance and speed) are not revealed by HP for intellectual property reasons.<sup>[25,33]</sup> The layer height was set at 80  $\mu\text{m}$ , as recommended by the printer manufacturer.

Both machines operate in air environment. The effective build volume of Sharebot SnowWhite<sup>2</sup> machine (100 × 100 × 100 mm<sup>3</sup>)<sup>[31]</sup> is significantly smaller compared to HP Jet Fusion Series 5200

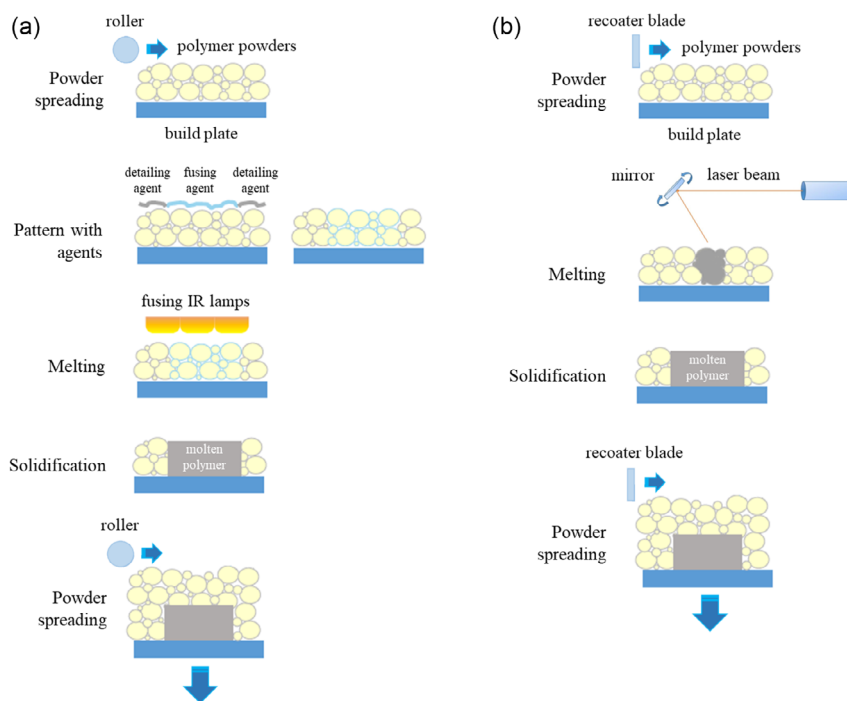


**Figure 1.** Schematic illustration of the working principle of the two PBF processes investigated: a) MJF and b) SLS.

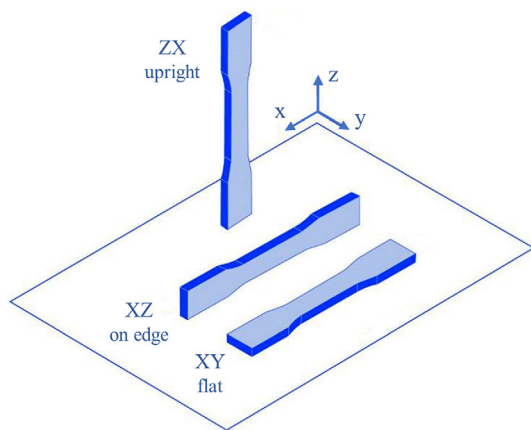


**Figure 2.** Schematic of the build orientations of the printed samples according to ISO/ASTM 52921.

( $380 \times 284 \times 380 \text{ mm}^{[13]}$ ) or other industrial SLS machines.<sup>[34]</sup> This difference in chamber sizes could influence the thermal history and cool-down time of the samples at the end of the printing process.

For each PBF process, dog-bone specimens according to ISO 527-2 standard (geometry 1BA) for tensile testing and rectangular bars complying ISO 178 and ISO 180 standards ( $80 \times 10 \times 4 \text{ mm}^3$  in size) for flexural and unnotched Izod impact tests were produced to compare their mechanical properties. Three build orientations, namely XY (“flat”), XZ (“on edge”), and ZX (“upright”) were chosen to evaluate the isotropy of the final parts (Figure 2). In addition, rectangular coupons ( $10 \times 10 \times 4 \text{ mm}^3$  in size) were fabricated for each orientation to evaluate the density of the printed parts by gas pycnometry.

Six tensile, six flexural, and ten Izod specimens were printed in the XY, XZ, and ZX orientations, respectively. A total of 66 parts were fabricated by MJF in one single job, while for SLS one job for each combination of mechanical test/print orientation was done due to the limited build volume of the machine. In both cases, the samples were allowed to cool down to  $50^\circ\text{C}$  before unloading the machine. The loose powder was removed from the fabricated parts using a brass brush and compressed air. MJF parts have a typical grayish look due to carbon black particles from the fusing agent.<sup>[21]</sup>

## 2.2. Characterization Techniques

The morphology, shape, and sizes of the feedstock powders were investigated using a ZEISS Merlin field-emission scanning electron microscope (FESEM) (Carl Zeiss Microscopy GmbH, Jena, Germany). FESEM analyses were also performed to observe the fracture surfaces of both SLS- and MJF-printed tensile samples to investigate the composite microstructure, the distribution of filler particles and their interfacial bonding with the polymer matrix as well as to identify failure mechanisms and processing defects (e.g., voids). The images were obtained using a wide magnification range (from  $60\times$  to  $5000\times$ ) using an accelerating beam voltage between 5 and 15 kV at high and low magnification,

respectively. A thin platinum layer was applied by sputter coating on every sample to avoid electrostatic charging effects.

The particle size distribution (PDS) of the powders was evaluated by examining several FESEM micrographs recorded at  $500\times$  magnification through Image J processing software. A total of 300 particles collected from 10 images were measured to obtain an accurate statistical evaluation of the PDS of the polymer particles. The same software and image analysis procedure was also used to determine the size distribution of the bare glass beads. However, in this case, a horizontal tube furnace (Nabertherm RHTC 80-710/15, Nabertherm GmbH, Lilienthal, Germany) was used to heat the powders up to  $800^\circ\text{C}$  in  $\text{N}_2$  atmosphere for 30 min to decompose the polymer matrix by pyrolysis. A small quantity of glass beads was then put onto a microscope slide and several images were collected at  $100\times$  magnification using a Leica DMI 5000 M optical microscope (Leica Microsystems GmbH, Wetzlar, Germany) to be analyzed.

Indirect measurements, such as bulk/tap density and static angle of repose (AOR), were performed to characterize the flowability of the powders, which is highly relevant for the recoating operations. In the former analysis, the apparent density ( $\rho_{\text{bulk}}$ ) of the test powder was obtained by filling a cylindrical container of known volume ( $25 \text{ cm}^3$ ). The tap density ( $\rho_{\text{tap}}$ ) was then evaluated by using a tapping procedure based on ASTM D7481-18.<sup>[35]</sup> From this test, the Hausner ratio (HR) can be obtained as:<sup>[35]</sup>

$$\text{HR} = \frac{\rho_{\text{tap}}}{\rho_{\text{bulk}}} \quad (2)$$

The flowing behavior of the powders was also evaluated by measuring the AOR in compliance with ISO 4324 standard. The test consists of loading the powders in a funnel and determining the height of a cone ( $h_{\text{AOR}}$ ) formed by powders flowing through the funnel orifice onto a circular plate of fixed diameter ( $d_{\text{AOR}} = 100 \text{ mm}$ ). The angle of repose  $\gamma$  was calculated as follows:<sup>[36]</sup>

$$\tan \gamma = \frac{2h_{\text{AOR}}}{d_{\text{AOR}}} = \frac{h_{\text{AOR}}}{50} \quad (3)$$

Each measurement has been repeated three times. These two parameters give qualitative information on the flowability and cohesion of powdered materials used as feedstock in PBF techniques.<sup>[35,36]</sup> Therefore, other glass beads reinforced PA12 powders specifically designed for SLS, such as PA 3200 glass filled (GF) and Duraform GF supplied by EOS GmbH (Krailling, Germany) and 3D Systems (Rock Hill, SC, USA) respectively, have also been tested for comparison.

The thermal transitions and the crystallinity of both virgin powders and printed parts were studied via differential scanning calorimetry (DSC) tests by using a PerkinElmer Pyris 1 instrument (PerkinElmer Inc., Waltham, MA, USA). Samples with a mass of  $10 \pm 1 \text{ mg}$  were tested in  $\text{N}_2$  atmosphere (flow rate at  $20 \text{ mL min}^{-1}$ ) following a standard heating-cooling cycle from  $25$  to  $230^\circ\text{C}$  at a rate of  $10^\circ\text{C min}^{-1}$ . PA 3200 GF and Duraform GF powders were also analyzed for the sake of comparison. Characteristic temperatures and enthalpy for melting and crystallization were determined from the DSC traces using



Pyris software. The crystalline degree ( $X_c$ ) of the PA12 matrix was calculated by Equation (4):

$$X_c = \frac{\Delta H_m}{\Delta H_{m0}(1-f)} 100 \quad (4)$$

where  $\Delta H_m$  is the melting enthalpy,  $\Delta H_{m0}$  denotes the reference value for the melting enthalpy of a fully crystalline PA12 ( $209 \text{ J g}^{-1}$  [37]), and  $f$  is the weight fraction of glass beads.

The thermal stability and the relative amount of filler were studied by thermal gravimetric analysis (TGA) through a Mettler Toledo TGA/SDTA851e instrument (Mettler Toledo, Columbus, OH, USA). To this end, samples of neat PA12 and PA12/GB were heated in alumina crucibles at  $10^\circ\text{C min}^{-1}$  from 25 to  $800^\circ\text{C}$  under argon atmosphere (flow rate at  $50 \text{ mL min}^{-1}$ ). The weight fraction of glass beads was evaluated from the difference between the final residues of the TGA curves of the reinforced and neat polymer.

The crystalline structure of the powders and printed samples was investigated by X-ray diffraction (XRD). A Panalytical PW3040/60 X'Pert PRO diffractometer equipped with a Cu- $K_\alpha$  X-ray source was used to conduct all experiments. The diffraction patterns were recorded at  $2\theta$  angular range of  $10^\circ$ – $60^\circ$  with a step size of  $0.013^\circ$ . The average sizes of sub-micrometer polymer crystallites in the direction perpendicular to the crystal plane that produces the diffraction peak ( $L$ ) were obtained by using Scherrer equation:

$$L = \frac{K\lambda}{\beta \cos \theta} \quad (5)$$

where  $K$  is a shape constant equal to 0.89, [18]  $\lambda$  denotes the wavelength of the incident X-ray beam ( $1.506 \text{ \AA}$  for the Cu- $K_\alpha$  source used),  $\beta$  is the full width of the diffraction peak at half maximum height, and  $\theta$  is the Bragg diffraction angle.

The density of the feedstock powders ( $\rho$ ) was obtained through a Ultrapyc 5000 gas pycnometer (Anton Paar QuantaTec, Boynton Beach, FL, USA) using helium as probing gas. Samples of powders having a mass of  $5 \pm 0.5 \text{ g}$  were tested following ASTM B923-20 standard. The density of the printed parts ( $\rho_{\text{printed}}$ ) was evaluated with the same instrument and procedure by testing five coupons with size of  $10 \times 10 \times 4 \text{ mm}^3$  for each orientation and technique. The porosity ( $\varphi$ ) of the printed samples was determined using Equation (6):

$$\varphi = \frac{\rho - \rho_{\text{printed}}}{\rho} 100 \quad (6)$$

The mechanical properties of the printed parts were characterized by means of tensile, flexural, and Izod impact tests. For tensile and flexural testing, MTS Criterion Model 43 universal testing machine (MTS Systems Corporation, Eden Prairie, MN, USA) equipped with a 5 kN load cell was used. The experiments were performed at a crosshead velocity of 2 and  $5 \text{ mm min}^{-1}$  for tensile and flexural tests, respectively. The international standards used as reference were ISO 527-2 and ISO 178. An extensometer with a gauge length equal to 25 mm was adopted to record elongation data during tensile testing. Izod unnotched impact tests were performed using an ATS Faar Impacts-15 instrument with a 2 J hammer according to

ISO 180. To improve the statistical significance of the results, at least 5 samples were tested for each technology and build orientation for tensile and flexural properties characterization. Similarly, 10 samples were used for impact analysis. All mechanical tests were performed at room temperature and the samples were previously dried in oven at  $80^\circ\text{C}$  for 6 h to eliminate moisture.

### 3. Results and Discussion

#### 3.1. Feedstock Characterization

Suitable particle shape and size distribution are highly important for the processability of polymeric powders by using PBF techniques. The morphology and surface structure of PA12/GB powders are illustrated in Figure 3.

The powders are a mixture of polyamide particles and glass beads as reinforcing filler. The polymeric particles showed rather homogeneous dimensions between 30 and  $90 \mu\text{m}$ , nearly elliptical or “potato” shapes and rough surfaces (Figure 3a,b). These characteristics can be attributed to the synthesis method (i.e., dissolution–precipitation of polyamide granules in ethanol solution at high temperature) described by Evonik Industries AG in several patents. [38,39] This method has proven effective to optimize the morphological and thermal properties of the powders for SLS processing. [38–40] A few cracks and satellites also appear at the particle surface (Figure 3c). Although the formation mechanism of this surface structure is not yet fully understood, it has been assumed to be induced by solvent evaporation that occurs in the synthesis process. [41,42]

The glass beads are perfectly spherical and evenly distributed in the polymer particles (Figure 3c). Some spheres reveal a smooth surface with no or very little polymer residue on it (Figure 3c), while others are strongly embedded in the polymer matrix (Figure 3d). This observation and the analysis of the patent of Evonik about the production of composite powders based on PA12 matrix [38] suggest that the glass beads are likely added directly in the reactor during the dissolution–precipitation process with the aim of improving the dispersion and chemical bonding between the filler and the polymeric matrix.

The size distribution of the polyamide particles is unimodal with a median size ( $d_{50}$ ) of  $57 \mu\text{m}$  (Figure 4), which was in good agreement with previous publications on neat PA12 powders supplied by HP for the MJF technology. [10,12,26] Moreover, the fraction of fine particles (i.e.,  $d < 20 \mu\text{m}$ ) is well controlled and this is important to avoid particle adhesion and sticking on the recoater. [12] A small fraction of coarse particles with sizes beyond  $90 \mu\text{m}$  is also present (Figure 4). The size distribution of the glass beads is also unimodal, with a median size of  $31 \mu\text{m}$  (Figure 4).

The flowability of PA12/GB powders, assessed through tap density and angle of repose tests, is very good (Table 1). In fact, according to Carr's classification of flow behavior based on the angle of repose, it belongs to the free-flowing class. Although a direct comparison is not entirely valid due to slight differences in glass beads content (Table 1) and size distribution, [43] it is worth noting that the flowability of PA12/GB powders is even better with respect to commercial glass beads-reinforced PA12 powders

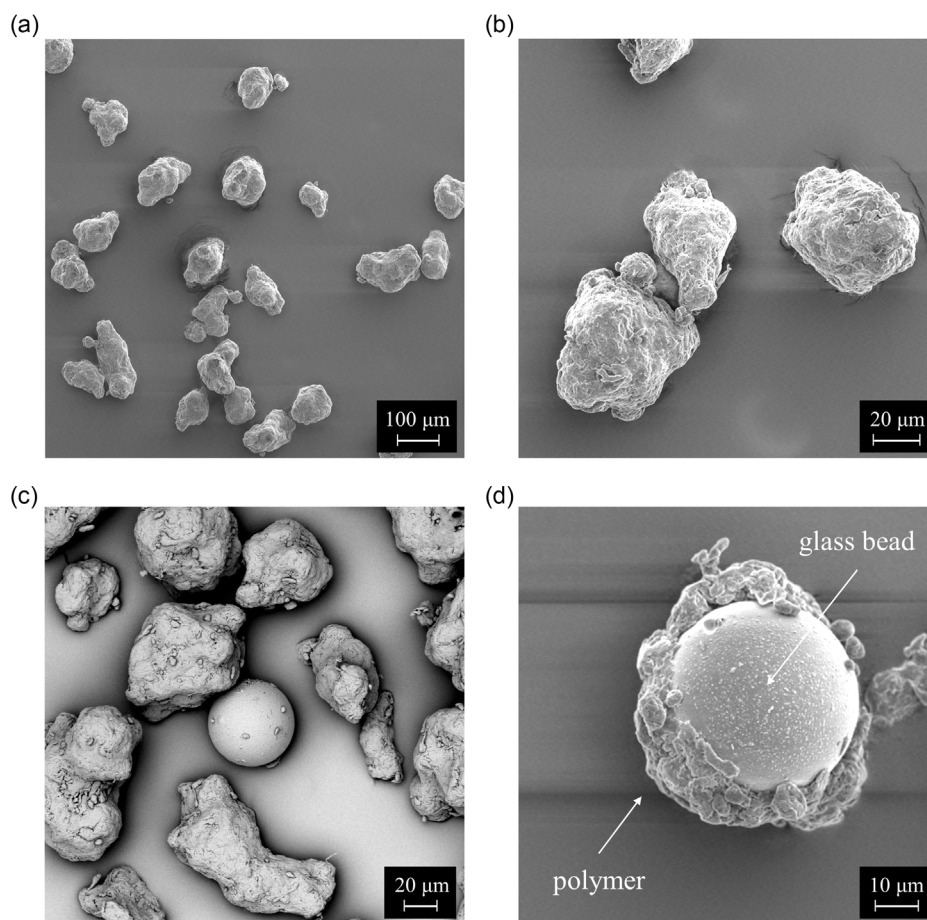


**Figure 3.** a–c) FESEM images showing the morphological features of PA12/GB powders: size, shape, and surface structure of polymer particles and d) reinforcing phase.

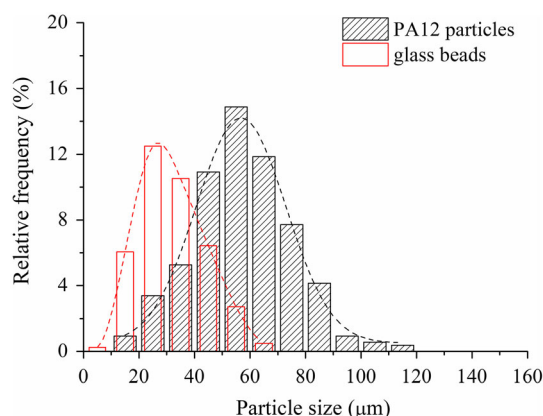


**Figure 4.** PDS of PA12/GB powders.

designed for the SLS process. In fact, Duraform GF and PA3200 GF exhibit higher Hausner ratio and angle of repose (Table 1). These results suggest that PA12/GB powders are expected to perform well in the SLS processes too since the ideal particle morphology, dimensional range, and flowability for ensuring

the spreading of a dense and defect-free powder layer are respected.<sup>[1,4]</sup>

PA12/GB powders were analyzed by DSC to determine their characteristic thermal transitions and crystalline degree. The DSC thermograms of PA12/GB powders for MJF technology are illustrated in Figure 5a; in addition, the traces recorded for two glass-filled PA12 powders for SLS were also reported for ease of comparison.

All materials show a single sharp endothermic peak with similar melting temperatures (Figure 5a). The crystallinity of the powders, calculated from the melting enthalpy values according to Equation (4), is also comparable as it reaches 44.5%, 47.4%, and 46.5% for PA12/GB, Duraform GF, and PA3200 GF, respectively. Such a sharp and high melting peak is favorable to exploit the advantage of laser or fast-moving IR lamps, that deliver a huge amount of energy in a short time, and to avoid the partial melting of the particles in the vicinity of the printed part.<sup>[1,4]</sup> A wide interval between melting and crystallization events (i.e., between 27 and 30 °C), commonly referred as “sintering window,”<sup>[5]</sup> is also visible for all materials (Figure 5a) and it helps to inhibit or at least slow down the crystallization of the polymer during processing.<sup>[1,4]</sup> Overall, the DSC analysis showed that both MJF and SLS powders exhibited similar thermal properties,

**Table 1.** Density, filler content, and flow properties of HP 3D High Reusability PA12 glass beads powders for MJF and commercial glass beads-reinforced PA12 powders for SLS (in both names GF stands for glass filled).

Material	True density [ $\text{g cm}^{-3}$ ]	Glass content [wt%]	Hausner ratio	Angle of repose [°]
HP PA12/GB	$1.366 \pm 0.001$	40	$1.17 \pm 0.01$	$31.5 \pm 0.5$ (free flowing)
Duraform GF	$1.406 \pm 0.001$	43	$1.21 \pm 0.01$	$33.0 \pm 0.4$ (free flowing)
PA3200 GF	$1.486 \pm 0.001$	50	$1.23 \pm 0.01$	$36.0 \pm 0.6$ (free flowing)

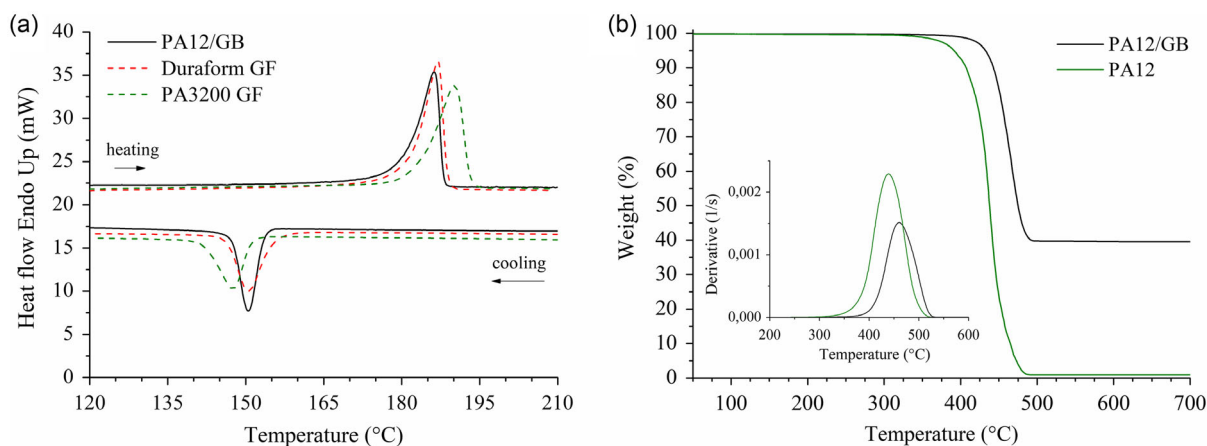


**Figure 5.** a) Comparison between the DSC curves of PA12/GB, Duraform GF, and PA3200 GF powders and b) TGA analysis in inert atmosphere of PA12/GB and neat PA12 powders supplied by HP for MJF technology, showing the high thermal stability and the filler content of the reinforced material.

which can be attributed to the specific fabrication method of PA12 powders produced by Evonik.<sup>[38,39]</sup> Although the details of the synthesis route are confidential, a comparable thermal behavior (Figure 5a) may suggest that similar parameters (e.g., thermal cycle and pressure) were adopted in the dissolution–precipitation process.

In addition to the calorimetric properties, the thermal stability of PA12/GB powders was investigated by TGA analysis. As shown in Figure 5b, neat and reinforced PA12 powders exhibited a single-step degradation starting at 345 and 398 °C, respectively. This noticeable increase in the onset degradation temperature of the reinforced powders can be attributed to the effect of the glass beads.<sup>[30]</sup> The decomposition of the polymer ended at 500 °C in both cases. The difference between the final residue of neat PA12 and PA12/GB powders that yield the glass beads content is 38.7 wt%. This value is in good accordance with that declared by the material supplier (40 wt%).<sup>[44]</sup>

### 3.2. Printed Parts Characterization

#### 3.2.1. Porosity

The densities of PA12/GB samples produced by MJF and SLS techniques, and tested by gas pycnometry, were in the range from 1.28 and 1.31  $\text{g cm}^{-3}$  and 1.32 and 1.34  $\text{g cm}^{-3}$ , respectively. This leads to some residual porosity quantified between 4 and 6.5% for MJF parts and 2.3 and 3.2% for SLS ones depending on the build orientation adopted, as shown in Table 2. Similar

**Table 2.** Porosity of SLS and MJF parts printed with different build orientations calculated using Equation (6), based on the comparison between gas pycnometer measurements on raw powders and 3D-printed samples.

Sample orientation	Manufacturing process	Porosity [%]
XY	SLS	$2.3 \pm 0.1$
–	MJF	$5.8 \pm 0.2$
XZ	SLS	$2.7 \pm 0.1$
–	MJF	$6.5 \pm 0.2$
ZX	SLS	$3.2 \pm 0.2$
–	MJF	$4.0 \pm 0.1$

values were reported in several studies for GF-reinforced SLS and MJF parts.<sup>[45–49]</sup>

MJF technique typically exhibits lower densities compared to SLS (Table 2). This is likely due to the evaporation of the aqueous solvent of the printing agents deposited during the fabrication process.<sup>[26]</sup> Specifically, the evaporation of water could promote pore formation by air entrapment or by a local cooling effect due to the removal of the evaporation energy that could hamper full coalescence of the polymeric powders.<sup>[9,26]</sup> However, whether SLS or MJF gives higher part density is still controversial in the literature since it may also depend on the process parameters adopted to produce the parts (i.e., laser power, scan speed, and



scan spacing for SLS and print profile and lamps irradiance for MJF), that are strictly confidential for MJF.<sup>[25,32,33]</sup> For example, Xu et al.<sup>[10]</sup> found a lower amount of porosity in neat PA12 samples produced by SLS, while Abbott et al.<sup>[16]</sup> got the opposite results; other authors<sup>[25,26]</sup> reported similar values for both techniques.

It is also worth noting that the samples printed by SLS in ZX direction show lower void content compared to the other two orientations (Table 2). Different explanations were suggested in literature to justify this trend such as the additional weight of the printed layers on previous ones as the part height increases,<sup>[29]</sup> a poor intralayer powder packing in the horizontal plane since no compaction force is applied during layer spreading<sup>[50]</sup> and differences in the number of IR exposure steps.<sup>[50]</sup> The authors suggest that the poor packing behavior of the polymer particles in the horizontal plane has, indeed, a negative effect on how powder fusion takes place. In fact, the fusing agent, due to its aqueous nature and good wetting properties provided by surfactants and organic cosolvents, easily penetrates the powder layer via the voids between them.<sup>[8]</sup> This allows for greater heat transfer in the z direction compared to the XY plane, leading to higher porosity for XY and XZ samples due to their larger cross-sectional area (800 and 320 mm<sup>2</sup> respectively) compared to ZX counterparts (40 mm<sup>2</sup>) (Figure 2). Differently, the SLS sample built in ZX direction exhibits higher porosity with respect to the other orientations (Table 2), which could be deleterious for the mechanical performances by causing an early failure.<sup>[27]</sup>

### 3.2.2. Mechanical Properties: Tensile and Flexural Tests

The mechanical properties of SLS- and MJF-printed specimens were compared by means of tensile and flexural tests. Typical stress–strain curves resulting from the tensile tests are graphically shown in Figure 6, while Table 3 summarizes the average values and standard deviations of the tensile properties obtained by testing five dog-bone specimens.

All samples exhibit similar stress–strain response with a reversible linear elastic segment at low stresses followed by nonlinear behavior (i.e., strain hardening) until rupture at low elongation at break values (Figure 6). Strain hardening is more visible in MJF samples, although the transition zone between elastic and plastic behavior is not clearly distinguishable (Figure 6b).

The SLS specimens built along the XY and XZ orientations have almost the same ultimate tensile strength (UTS) and elongation at break, while the ZX orientation shows a significant reduction of these properties, equal to 32% and 60%, respectively (Figure 6a and Table 3). By contrast, only minor differences in the tensile properties were observed between MJF samples built in the three orientations. However, it is worth noting that MJF samples built in the ZX orientation exhibit a slight enhancement in both elastic modulus and tensile strength when compared to XY- and XZ-built directions. This increase follows the sequence XY < XZ < ZX (Figure 6b and Table 3), similar to what was observed in early works on neat PA12.<sup>[15,48]</sup> The elongation at break does not significantly change among the three orientations

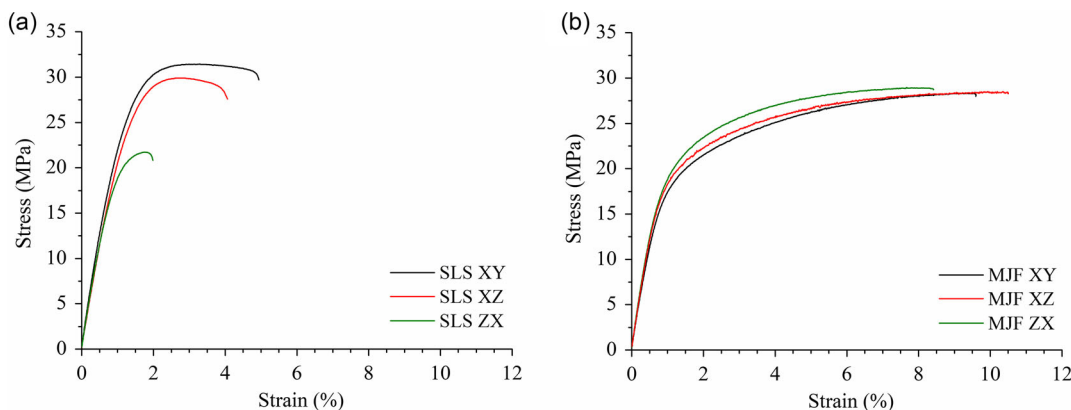


**Figure 6.** Representative tensile curves of PA12/GB samples printed along different build orientations: a) SLS and b) MJF.

**Table 3.** Average values and standard deviations of tensile and flexural properties of SLS and MJF samples printed with different build orientations.

Sample orientation	Manufacturing process	Elastic modulus [MPa]	Tensile strength [MPa]	Elongation at break [%]	Flexural modulus [MPa]	Flexural strength [MPa]
XY	SLS	2317 ± 192	31.0 ± 0.6	4.4 ± 1.7	2432 ± 107	61.3 ± 2.0
–	MJF	2307 ± 114	28.5 ± 0.4	9.7 ± 0.9	2314 ± 192	48.4 ± 1.2
XZ	SLS	2635 ± 106	31.0 ± 1.2	3.9 ± 0.7	2594 ± 56	59.5 ± 1.1
–	MJF	2444 ± 67	28.7 ± 0.1	10.6 ± 1.0	2201 ± 147	48.0 ± 1.4
ZX	SLS	2379 ± 136	21.0 ± 2.3	1.7 ± 0.5	2236 ± 110	44.0 ± 4.7
–	MJF	2566 ± 145	29.6 ± 0.6	8.7 ± 0.9	2576 ± 90	53.9 ± 0.7

in MJF parts (Table 3). This is coherent with the data reported in refs. [8,29] for neat and glass bead-reinforced PA12 parts.

The tensile strength of SLS parts built in the XY and XZ orientations is almost 10% higher compared to MJF ones (Table 3). By contrast, the UTS of the MJF-printed specimens built in the ZX orientation was 40% higher than that of SLS-printed counterparts (Table 3). This suggests that the ZX samples have higher tensile properties when processed by MJF; this is an opposite trend if compared to what has been observed in SLS (Figure 6 and Table 3). Moreover, MJF samples exhibit a more ductile behavior showing elongation at break values that are from about twice (for XY and XZ orientations) to five times (for ZX one) higher than the SLS counterparts (Figure 6 and Table 3). These overall results are in high agreement with previous findings on neat PA12 parts.<sup>[12,25]</sup>

Representative stress–strain curves recorded by flexural tests are shown in **Figure 7** and the values of the corresponding modulus and strength are reported in Table 3.

The flexural properties' tendency as a function of the build orientations was the same as the tensile properties' for both technologies; in fact, the ZX orientation displays the weakest and highest performances for SLS and MJF samples, respectively (Figure 7 and Table 3). Similar flexural properties of MJF-printed PA12/GB parts were found by O'Connor et al.<sup>[14]</sup> who reported flexural modulus of around 2300 MPa and strength between 50 and 59 MPa depending on the build orientation. In the case of SLS technique, the specimens fabricated in the ZX orientation show significantly reduced strain at break compared to those printed along the XY and XZ ones (60% and 40% decrease, respectively) (Figure 7a and Table 3). This confirms that the SLS parts became more brittle when printed in the vertical direction.

Since significant differences in mechanical behavior arose between SLS and MJF samples, a detailed discussion of the results will be done in the following: 1) Samples printed by SLS and MJF show a certain degree of mechanical anisotropy, which is correlated to their porosity. The SLS process provides a better flexural and tensile behavior for XY and XZ samples (Table 3) due to the lower voids content compared to ZX ones (Table 2). Moreover, in ZX parts, the applied stress is normal to the layer interfaces, which are usually weak.<sup>[34,40]</sup> This behavior agrees with that generally observed in the literature.<sup>[34]</sup> By

contrast, MJF ZX samples exhibit improved modulus and strength compared to the XY and XZ ones (Table 3) as a result of the lower porosity level (Table 2). 2) The SLS process allows to obtain of samples showing better mechanical properties compared to MJF (in XY and XZ orientations) due to the lower porosity of the produced samples (Table 2 and 3).<sup>[10]</sup> The occurrence of postcondensation reactions in SLS due to the higher preheating temperature and the consequent increase of the polymer's molecular weight could also play a role in this aspect.<sup>[12,20]</sup> By contrast, MJF parts exhibit higher performances in the ZX orientation compared to SLS ones (Table 3) due to a stronger bonding between layers, that derives from two typical characteristics of MJF technology.<sup>[20,26]</sup> First, the planar IR radiation leads to a more homogeneous heat distribution compared to the line scanning strategy employed in SLS.<sup>[20,26]</sup> Second, the proprietary fusing agent promotes an efficient heat transfer in the Z direction upon exposure to IR radiation due to the high absorptivity of the carbon black and the good wettability provided by the organic additives (i.e., surfactants and cosolvents).<sup>[8,20,26]</sup> Both these factors lead to better integrity of layer interfaces.<sup>[8,15]</sup> These favorable conditions are not met in the SLS process, where the adhesion between layers is guaranteed by polymer viscous flow only.<sup>[1,4]</sup> 3) The flexural behavior is more susceptible to the presence of voids with respect to the tensile one, as revealed by comparing Table 2 and 3. In fact, the difference in flexural strength between SLS and MJF parts built along XY and XZ directions is more than doubled with respect to the tensile strength (Table 3). Similar observations were also reported by previous studies on 3D-printed PA12 parts fabricated along different orientations.<sup>[14,27]</sup>

### 3.2.3. Impact Strength

A comparison of Izod impact strength between the different processes and build orientation is reported in **Table 4**. The impact strength of the samples, tested in unnotched configuration, is significantly the same for both techniques, except for ZX-oriented SLS parts. In fact, no clear differences can be detected when comparing SLS and MJF parts across XY and XZ orientations as well as between these two orientations in the same technique (Table 4). This isotropic behavior is

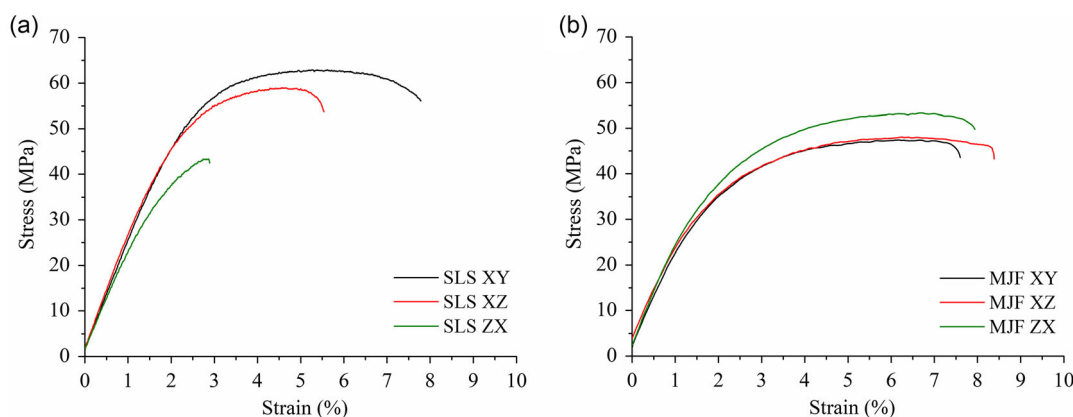


**Figure 7.** Representative flexural curves of PA12/GB samples printed along different build orientations: a) SLS and b) MJF.

**Table 4.** Izod impact strength of SLS and MJF samples printed with different build orientations.

Sample orientation	Manufacturing process	Izod impact strength [ $\text{kJ m}^{-2}$ ]
XY	SLS	$10.0 \pm 1.2$
–	MJF	$9.1 \pm 0.7$
XZ	SLS	$10.1 \pm 1.6$
–	MJF	$8.8 \pm 1.0$
ZX	SLS	$5.4 \pm 0.4$
–	MJF	$9.2 \pm 1.1$

preserved in the upright orientation also for MJF technique, while for SLS a significant reduction of impact strength (about 45%) was recorded in this direction (Table 4). This happens because, in MJF, the fusing agent helps to obtain better interlayer melting and adhesion compared to what is possible to achieve with SLS.<sup>[12]</sup> Moreover, the effect of the low interlayer strength in ZX-oriented SLS parts is further amplified by the test configuration as the impact direction is parallel to building plane and thus the interlayer interfaces.

### 3.2.4. Surface Fractures of Tensile Samples

The fracture surfaces of PA12/GB specimens built by SLS and MJF processes after tensile tests were observed by FESEM. All samples exhibited similar failure mechanisms regardless of the build orientation; as an example, **Figure 8** reports representative images of the XZ-oriented parts. The fracture mechanism is primarily brittle, with some regions of ductile failure (Figure 8a,b). In fact, one end of the fracture surfaces of SLS and MJF tensile dog-bones clearly displays the morphology of

ductile failure with evident plastic deformation (Figure 8a,b). This region meets with a much larger and smoother part where brittle failure occurs, as visible in Figure 8a,b where the transition zone is outlined by a dashed line. These microstructural features were already observed by O'Connor et al.<sup>[29]</sup> on the same material processed by MJF and by Seltzer et al.<sup>[45]</sup> and Liu et al.<sup>[51]</sup> on PA12/GB parts processed by SLS. From a comparison among the two processes, the ductility is greater for MJF specimens, as revealed by the more extended plastic deformation region in the fracture surface (Figure 8a). This means that a greater amount of energy is absorbed before failure, leading to higher elongation at break values with respect to SLS parts (Table 3), that usually exhibit a much flatter fracture surface (Figure 8a).<sup>[34,45,51]</sup> A small number of spherical voids is present on the fracture surfaces of the samples processed by both techniques (Figure 8a,b).

Figure 8c clearly displays the existence of a dividing boundary between the ductile region, where crack nucleation and stable growth occur, and the brittle region, where the crack rapidly propagates until catastrophic failure. The high-magnification micrographs shown in Figure 8d,e provide examples of these two types of failure mode. The cracks originate and grow from the interfaces between the glass beads and the polymer matrix, resulting in a clear separation between them (Figure 8d). Consequently, the applied stress is carried out by the PA12 matrix only, thus leading to stress concentration in the polymer surrounding the glass beads, that further promotes crack growth. Therefore, the filler/matrix interfaces are the main pathways of crack growth.<sup>[51]</sup> The severe plastic deformation of the polymer that takes place at these interfaces is well captured in Figure 8d. Since the cracks growth in this stage is slow, the different mechanical behavior of the polymer matrix (i.e., high ductility) and the glass beads (i.e., rigid filler) can be clearly recognized in the failure process and the corresponding fracture surface

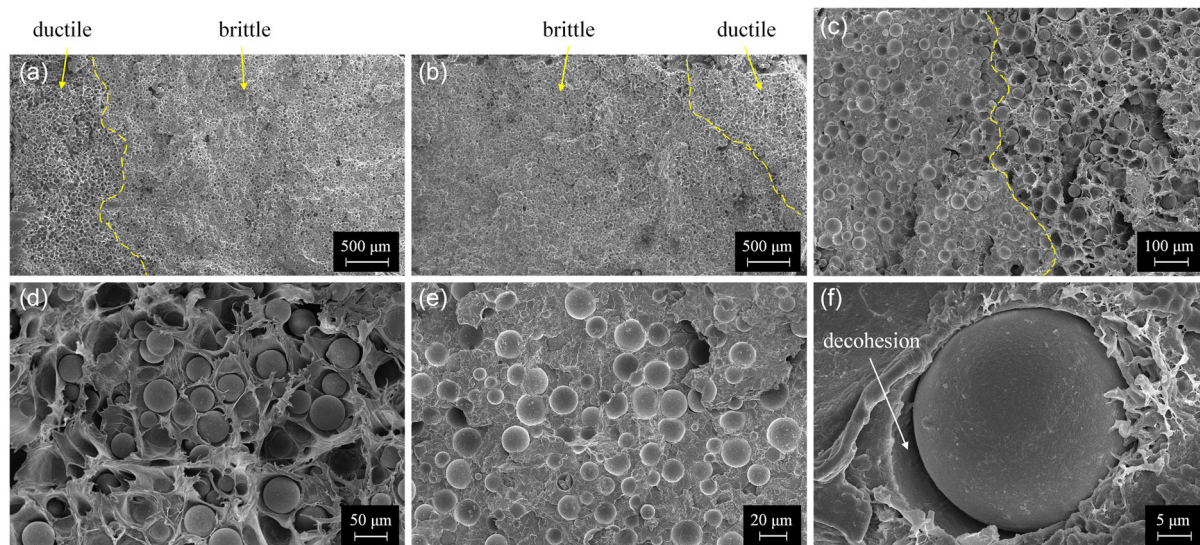


**Figure 8.** FESEM micrographs of the fractured surfaces of PA12/GB parts processed by SLS and MJF technologies. Typical fracture surface of a) MJF and b) SLS samples after tensile testing demonstrating ductile/brittle failure modes; c) transition zone between ductile (right) and brittle (left) regions; high magnification images of d) ductile and e) brittle regions; f) representative interface between the polymer matrix and a single glass sphere showing decohesion and polymer plastic deformation.



is rather rough and fibrous (Figure 8d). The existence of holes in the polymer matrix, where the glass beads have been detached, as well as the decohesion and smooth surface morphology of the remaining filler particles indicates a poor wettability and interfacial adhesion between the matrix and the reinforcing phase (Figure 8d).<sup>[29]</sup> When one crack reaches a critical size, rapid propagation and brittle failure occur. In this region, the fracture surface becomes relatively smooth and no apparent fibrous-like deformation is visible (Figure 8e). Note what visually appears to be again detachment and poor adhesion between the filler particles and the polymer matrix (Figure 8e). The decohesion between a single glass bead and the polymer as well as the plastic deformation near the interface are further highlighted in Figure 8f. In view of these observations, the authors suggest that the enhancement of the glass/matrix interfacial adhesion by surface modification is needed to improve mechanical properties.<sup>[29,46]</sup>

### 3.2.5. Microstructure: Thermal and XRD Analysis

A detailed analysis of the material microstructure and crystalline phases typical of MJF and SLS parts is illustrated in Figure 9 by comparing XRD patterns, DSC thermographs, and FESEM images. The analyses performed on the powders before processing are also reported in the XRD and DSC graphs in Figure 9a,b, d,e as dashed curves for ease of comparison.

After MJF or SLS processing, PA12/GB parts had a main characteristic diffraction peak at approximately  $21.6^\circ$ , that corresponds to a stable  $\gamma$ -crystal form (001) (Figure 9a,d). Differently, in the feedstock powders, two peaks at  $21^\circ$  and  $22.1^\circ$  appear that

match metastable crystal modifications of  $\gamma$  (001) and  $\gamma$  (200) plane, respectively (Figure 9a).<sup>[52,53]</sup> These changes in the crystalline structure are also visible in the DSC traces as the printed samples exhibit peak broadening and translation to lower melting temperatures compared to the feedstock powders (Figure 9b,e).

As described in previous works,<sup>[25,26,41]</sup> the difference in melting temperature between powders and sintered parts is induced by changes in the morphology of the crystalline phases. In fact, during both PBF processes, high powder bed temperatures are used for the entire building job to avoid warpage and thermal distortion of the parts, that subsequently cools down and crystallize at slow cooling rates and ambient pressure. These conditions allow the crystalline chains to form a stable  $\gamma$ -phase; in addition, a significant drop in crystallinity was observed if compared to the metastable  $\gamma$ -structure which is induced by high-pressure crystallization during the dissolution–precipitation process adopted for producing the raw powders (Figure 9b,e).<sup>[52,53]</sup> The changes in the crystalline structure between powders and the printed parts built along the various orientations, derived by XRD and DSC analysis, are summarized in Table 5.

Small differences emerge between samples built through the two technologies in terms of DSC thermographs (Figure 9). MJF parts exhibit a double-endotherm pattern with a low-temperature melting peak ( $T_{pm1}$  in Table 5) at  $179\text{--}180^\circ\text{C}$  and a smaller high-temperature shoulder ( $T_{pm1}$  in Table 5) at  $186^\circ\text{C}$  corresponding to the LT- $\gamma$  and HT- $\gamma$  phases, respectively (Figure 9b). The formation of this shoulder can be attributed to an inhomogeneous and bimodal melting of the polymer matrix evidenced by the presence of spherulite nuclei with a higher melting temperature than

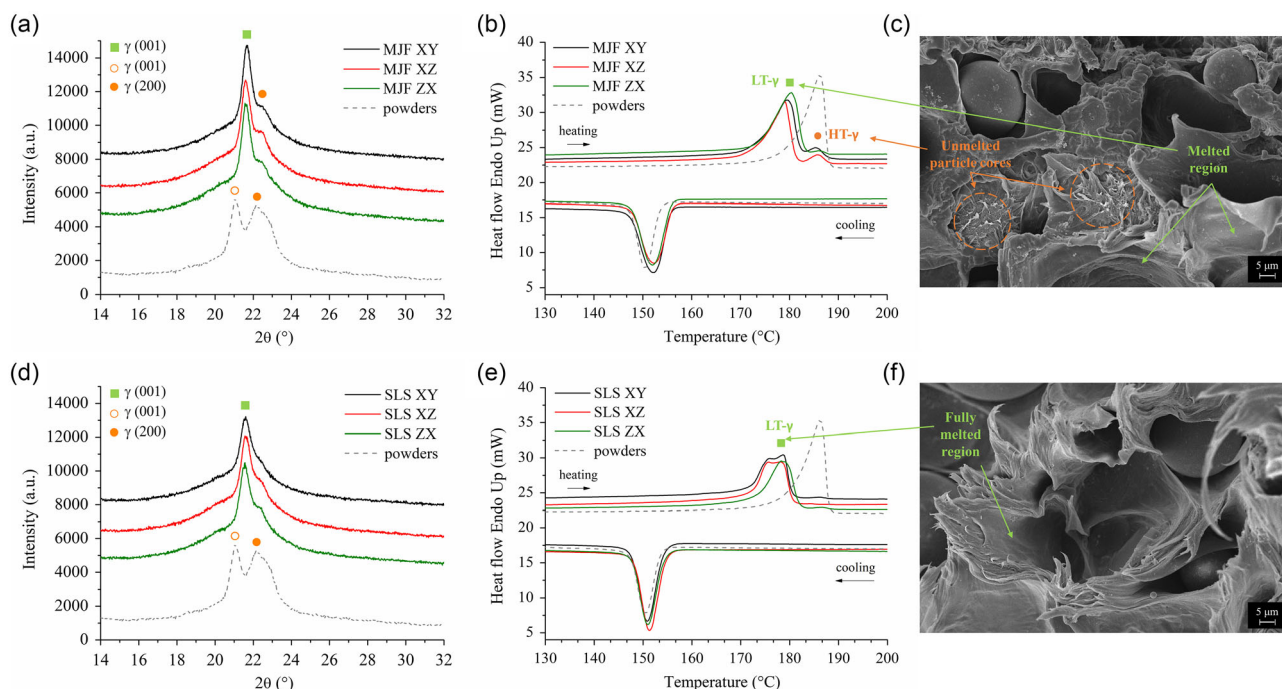


**Figure 9.** Phase analysis combining XRD, DSC, and FESEM images of the microstructure of MJF and SLS samples printed along different built orientations. For MJF samples: a) XRD patterns, b) DSC traces, and c) FESEM image of the tensile fractured surfaces of a typical cross section. For SLS samples: d) XRD patterns, e) DSC traces, and f) FESEM image of the tensile fractured surfaces of a typical cross section.



**Table 5.** Quantitative comparison of the microstructural and thermal properties of raw powders, SLS- and MJF-printed samples. The diffraction peaks  $\gamma$  (001) and  $\gamma$  (200) and the average crystallite size ( $L$ ) were determined from XRD patterns. Peak melting temperatures ( $T_{pm1}$  and  $T_{pm2}$ ) and enthalpy ( $\Delta H$ ), peak crystallization temperature ( $T_{pc}$ ) and crystalline degree ( $X_c$ ) were calculated from DSC curves. Note that in MJF parts  $T_{pm1}$  and  $T_{pm2}$  correspond to the fully melted region of the polymer powders and unmelted particle cores, respectively.

Sample	$\gamma$ (001) [ $2\theta$ ]	$\gamma$ (200) [ $2\theta$ ]	$L$ [nm]	$T_{pm1}$ [°C]	$T_{pm2}$ [°C]	$\Delta H$ [J g <sup>-1</sup> ]	$X_c$ [%]	$T_{pc}$ [°C]
Powders	21.02	22.08	–	186.2	–	57.1	44.5	150.5
MJF – XY	21.62	22.59	11.3	179.6	185.6	36.5	28.4	152.2
MJF – XZ	21.60	22.51	10.7	179.1	185.7	35.0	27.3	152.3
MJF – ZX	21.57	22.51	10.8	180.4	185.9	35.5	27.7	152.0
SLS – XY	21.61	–	8.4	178.6	–	28.8	22.4	150.9
SLS – XZ	21.56	–	8.1	178.1	–	29.2	22.8	151.4
SLS – ZX	21.57	–	8.2	178.3	–	29.9	23.3	150.9

the surrounding crystalline phase (Figure 9b,c).<sup>[54,55]</sup> The high-magnification FESEM image of the interiors of the MJF parts shows this nonuniform crystalline structure (Figure 9c). Most portion of the polymer particles are fused by the infrared lamps (LT- $\gamma$  in Figure 9b), except little spherulite nuclei that correspond to the unmelted cores of PA12 particles (i.e., HT- $\gamma$  in Figure 9b), as revealed by the fact that the shoulder peak temperature ( $T_{pm1}$  in Table 5) is very close to the melting peak temperature of the raw powders (Figure 9b). This means that the polymeric powders did not absorb enough energy to fuse completely when MJF parts are built in along the XY and XZ orientations.<sup>[20,26]</sup> In fact, the fusing agents coat the polymeric powders due to their particular wetting behavior and promote more efficient heat transfer at the interfaces between particles compared to their inner region. This unique melting behavior was reported by various authors for neat PA12 parts manufactured via MJF.<sup>[10,16,28]</sup> A negligible peak appears for ZX orientation, thus the existence of unmelted particle cores in this case is inconspicuous.<sup>[10]</sup> This validates the hypothesis of better heat propagation along Z axis and thus improved melting for vertically oriented MJF parts due to the specific properties of the fusing agent (see Section 3.2.2). The presence of unmelted particle cores in XY and XZ samples may negatively influence the strength of the final parts. This is in agreement with previously reported mechanical results which evidence a better flexural and tensile behavior for ZX samples fabricated by MJF with respect to XY and XZ ones (Table 3).

By contrast, SLS samples yield thermograms with a single broad endotherm centered around 178 °C (Figure 9e and Table 5). This suggests that a complete melting of the polymeric particles occurs during the SLS process thanks to the high energy supplied by the laser beam. The FESEM image in Figure 9f shows that the powders have been almost entirely fused due to the powerful instant heating capability of the CO<sub>2</sub> laser, with no observable unmelted spherulites.<sup>[10,16,28]</sup> Note that the melting peak of the SLS parts built in the XY and XZ orientations exhibits a small shoulder at slightly lower temperature compared to the characteristic melting peak (Figure 9e). This behavior can be ascribed to the presence of two distinct crystal populations in terms of lamellae shape and thickness or to a melting–recrystallization–remelting mechanism.<sup>[56]</sup>

To corroborate this analysis, the XRD patterns of the printed parts are compared in Figure 9a,d. The distinct peak of  $\gamma$  (001) plane appeared for all the samples investigated in this work with

almost identical peak position and modest differences in peak intensity (Figure 9a,d and Table 5). However, the presence of unmelted particle cores in MJF parts brings a small bulge near the main peak at 22.5° corresponding to the  $\gamma$  (200) phase found in the raw powders (Figure 9a). The crystallite size, calculated using Equation (5), is slightly larger for MJF parts (Table 5).

The crystallinity degree found from DSC curves according to Equation (4) is higher for MJF (about 28%) compared to SLS parts (about 23%) (Table 5). This finding will correspond with the thermal analysis carried out by previous studies on neat PA12 fabricated parts.<sup>[10,25]</sup> Moreover, it is worth noting that the samples with higher crystalline degrees generally exhibit a larger crystallite size, as shown in Table 5. These microstructural differences are probably a consequence of the different thermal history and cool-down time between the two techniques.<sup>[10,12]</sup> In fact, the larger build chamber volume (see Section 2.1) and the higher temperature of the build plate<sup>[8]</sup> of the MJF system result in a cooling rate estimated as 0.2 °C min<sup>-1</sup>.<sup>[8,18]</sup> Instead, the smaller build chamber of SLS machine induces a faster cooling,<sup>[57]</sup> with rate approaching 2 °C min<sup>-1</sup>. This means that MJF parts experienced lower cooling rate and longer residence time at elevated temperature during cooling, that definitely promote crystal growth.<sup>[10,17,23,25]</sup> The print job configuration adopted in this study (i.e., single job for MJF against different jobs for SLS in reasons of the large difference in the size of the build chamber of the machine used) could also play a role as generally print jobs with higher total number of layers exhibit longer cooling time.<sup>[58]</sup>

The crystallization peak in both powders and parts is relatively sharp and narrow (Figure 9b,e). The nucleating effect of the carbon black contained in the fusing agent, already observed by other authors,<sup>[20]</sup> is confirmed here by comparing the cooling curves of MJF and SLS samples (Figure 9b,e). The MJF specimens crystallize at higher temperatures (about 1 °C for both onset and peak temperatures, see Table 5) than the SLS counterparts across all orientations because carbon black particles act as nucleation sites and advance the crystallization of the polymer.<sup>[26]</sup>

### 3.3. Process/Material Comparison

Glass beads-reinforced PA12 is a popular material choice for PBF processes due to improved stiffness, dimensional stability, and heat resistance combined to ease of processing. The tensile

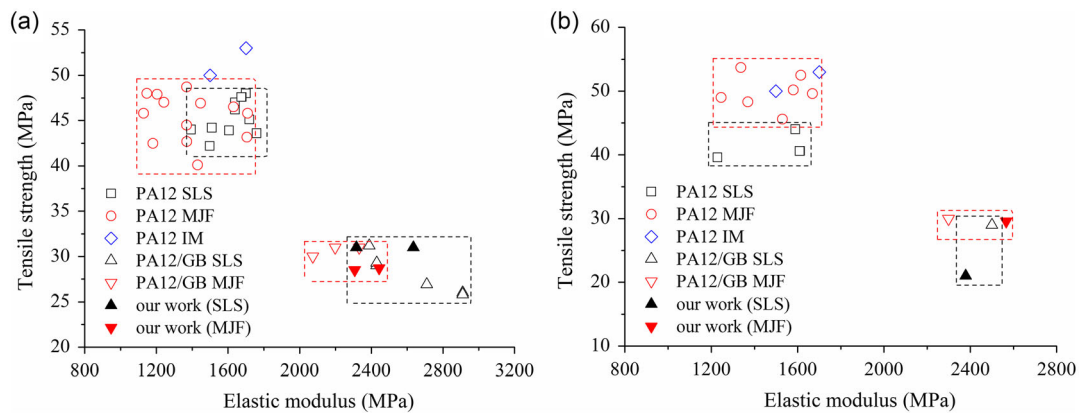


**Figure 10.** Comparison between experimental and literature data for tensile properties (strength vs stiffness) of neat PA12 and PA12/GB parts manufactured by PBF processes and IM: a) samples printed along the build plane, meaning flat and on-edge configuration as described in Figure 2 (XY/XZ orientations) and b) samples built along the vertical direction (ZX orientation). Legend: MJF, SLS, IM. The results obtained in this work are outlined with solid fill symbols. See Table A1 in the Appendix Section for details about all literature data reported in the figure (manufacturing technique, material, filler content, elastic modulus, and tensile strength values, authors).

properties of PA12/GB parts obtained in this study are therefore benchmarked against literature values. **Figure 10** provides a graphical overview of the tensile modulus and strength of neat PA12 and glass beads-reinforced PA12 parts produced by SLS and MJF technologies as well as injection molding (IM), based on the data acquired from various studies (for details see Table A1 in the Appendix Section). The mechanical properties obtained in this work (outlined by fill symbols) are in good agreement with those reported in literature for the same material and AM technique (Figure 10).

Due to differences in types of manufacturing technique, process parameters, and filler content, a fully quantitative and direct comparison is difficult to make. However, based on collected results, the following comments can be drawn: 1) PA12/GB composites exhibit enhanced stiffness but reduced mechanical strength compared to unreinforced PA12 counterparts (Figure 10). In fact, a 60% average improvement of elastic modulus (values between 2300 and 3000 MPa) and 30% average decrease in tensile strength (values of about 30 MPa) can be found by comparing our data and those found in literature (Figure 10). 2) The mechanical properties of PA12/GB parts produced by SLS in this work are in good agreement with respect to those obtained in several studies using commercial powders specifically developed for SLS.<sup>[45,46,59]</sup> 3) PA12/GB parts printed using MJF process show mechanical properties comparable with those obtained using SLS, although slight differences exist when comparing the various orientations. In fact, MJF parts generally have higher mechanical isotropy compared to SLS.<sup>[12,15,25–27]</sup> Moreover, SLS samples built in the upright (ZX) direction show quite low mechanical performances due to limited interlayer bonding (Figure 10b).<sup>[12,26,40]</sup> However, they usually have superior stiffness and strength compared to MJF parts when the specimens are produced in the flat (XY) or on-edge (XZ) orientations.<sup>[10,12]</sup> 4) A closer look at the comparison between additively manufactured and injection molded PA12 parts shows little differences in the tensile performances (Figure 10).<sup>[60,61]</sup> This means that polymeric PBF processes could represent a

competitive alternative to conventional techniques for parts with complex geometries as well as small series production. However, the ductility of the materials issued from AM techniques is still significantly reduced compared to conventional counterparts in reason of the residual porosity induced by the consolidation mechanisms typical of the additive process.<sup>[62]</sup>

## 4. Conclusion

In the study, two industrially relevant polymeric PBF techniques, SLS and MJF, respectively, were systematically compared through an investigation of the thermophysical properties of the raw material (i.e., the same glass bead-reinforced PA12 powder) and a detailed analysis of the microstructure, mechanical behavior, and fracture mechanism of the parts printed along three characteristic build orientations.

The raw powders are a mixture of ellipsoid-shaped polymeric particles and 39 wt% glass spheres. The PDS, flowability, and thermal properties are well suited to guarantee robust processability with both printing techniques. Although specifically designed for the MJF process, HP 3D High Reusability PA12 GB powders can be successfully processed by SLS. In fact, the microstructure and mechanical properties obtained are similar to those reported in literature for commercial SLS powders.

A clear anisotropy in tensile, flexural, and impact properties was discovered for parts produced by SLS and to a lesser extent by MJF. However, the stiffness and strength tendency across the different build orientations are quite the opposite between the two techniques. In fact, SLS exhibits slightly higher performances in the XY and XZ orientations, while MJF clearly shows a property enhancement in the ZX orientation, reaching strength values as higher as 40% than those of the SLS counterparts in every load scenario. These differences can be attributed to the irradiation and consolidation mechanisms typical of the two processes, where the planar and more homogeneous energy input and the presence of the fusing agents in MJF ensure more effective melting and better interlayer adhesion in the ZX

direction. In contrast, the porosity content plays a role in determining the higher performances of SLS parts printed along the XY and XZ orientations.

Both SLS and MJF parts have identical phase constitution matching the  $\gamma$  (001) crystal form, but slight differences arise in their microstructure in terms of crystalline structure and morphology. In fact, MJF samples exhibit higher crystallinity and crystallite sizes compared to SLS ones as a result of the different thermal history and cooling rate. In addition, a bimodal endothermic signal is recorded in the DSC curves of MJF parts, while the corresponding SLS traces retain a single endothermic signal due to the more effective heating capability of the laser. In MJF parts, the second melting peak is quite evident for XY/XZ orientations only, thus justifying the higher melting efficiency of MJF for samples build along the vertical direction.

Finally, it is worth noting that the MJF process shows lower variations of mechanical properties between samples compared to SLS. Moreover, the printing speed is greatly raised due to the innovative sintering approach. This aspect is greatly relevant for future industrial applications and, combined with a substantial balance of mechanical performances compared to the

well-known SLS process, will further contribute to the development and market growth of MJF technology in the next years.

## Appendix

**Figure A1** Graphical representation of the build orientation of SLS and MJF samples listed in **Table A1**. Note that the recoater moves along the X-direction.

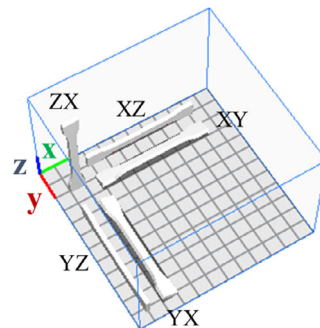


**Table A1.** Summary of literature data reported in Figure 10 showing the tensile properties of neat and glass beads reinforced PA12 parts manufactured by MJF, SLS, and IM. The build orientation defines the printing direction of the SLS and MJF parts within the build chamber according to the sketch of Figure A1.

Manufacturing technique	Material	Filler content [wt%]	Build orientation	$E$ [MPa]	$\sigma$ [MPa]	References
SLS	PA12/GB	40	XY	2430.0	29.0	[29]
SLS	PA12/GB	43	XY	2910.0	26.0	[29]
SLS	PA12/GB	43	XY	2710.0	26.9	[45]
SLS	PA12/GB	40	XY	2388.0	31.1	[59]
SLS	PA12/GB	40	XY	2430.0	29.3	[46]
–	–	–	ZX	2500.0	29.0	[46]
MJF	PA12/GB	40	XY	2074.0	30.0	[30]
MJF	PA12/GB	40	XY	2074.0	31.0	[29]
–	–	–	YZ	2198.0	31.0	[29]
–	–	–	ZX	2299.0	30.0	[29]
SLS	PA12	0	XY	1760.0	43.6	[10]
SLS	PA12	0	XY	1710.0	45.8	[16]
SLS	PA12	0	XY	1498.0	42.2	[28]
SLS	PA12	0	XY	1720.0	45.1	[63]
SLS	PA12	0	XY	1715.0	48.0	[60]
SLS	PA12	0	XY	1640.0	46.2	[64]
SLS	PA12	0	XY	1677.0	47.6	[12]
			ZX	1612.0	40.6	[12]
SLS	PA12	0	XY	1675.0	47.6	[40]
–	–	–	ZX	1610.0	40.6	[40]
SLS	PA12	0	XY	1640.0	47.0	[46]
–	–	–	ZX	1580.0	44.0	[46]
SLS	PA12	0	XY	1394.5	44.0	[26]
–	–	–	YZ	1605.4	43.9	[26]
–	–	–	ZX	1222.8	39.6	[26]
MJF	PA12	0	XY	1420.0	40.1	[10]

**Table A1.** Continued.

Manufacturing technique	Material	Filler content [wt%]	Build orientation	E [MPa]	$\sigma$ [MPa]	References
MJF	PA12	0	XY	1510.0	44.2	[16]
MJF	PA12	0	XY	1705.4	43.2	[23]
MJF	PA12	0	XY	1180.0	42.5	[30]
MJF	PA12	0	ZX	1530.0	45.6	[25]
MJF	PA12	0	XY	1446.0	46.9	[20]
–	–	–	ZX	1641.5	52.5	[20]
MJF	PA12	0	XY	1128.0	45.8	[12]
–	–	–	YX	1204.0	47.9	[12]
–	–	–	ZX	1337.0	53.7	[12]
MJF	PA12	0	XY	1369.0	48.7	[26]
–	–	–	YZ	1368.8	44.5	[26]
–	–	–	ZX	1669.2	49.6	[26]
MJF	PA12	0	XY	1242.0	47.0	[29]
–	–	–	YZ	1147.0	48.0	[29]
–	–	–	ZX	1246.0	49.0	[29]
MJF	PA12	0	XY	1370.0	42.6	[48]
–	–	–	YX	1630.0	46.5	[48]
–	–	–	ZX	1580.0	50.2	[48]
IM	PA12	0	–	1500.0	50.0	[60]
IM	PA12	0	–	1701.0	53.0	[61]

## Acknowledgements

This research did not receive any specific grant from funding agencies in the public, commercial, or not-for-profit sectors. The authors thank Mauro Raimondo for FESEM images, Michele Rosito for XRD analysis as well as Antonio Favero for the execution of the mechanical tests.

## Conflict of Interest

The authors declare no conflict of interest.

## Data Availability Statement

The data that support the findings of this study are available from the corresponding author upon reasonable request.

## Keywords

microstructure and mechanical properties, multi jet fusion, polymer composites, powder bed fusion, selective laser sintering

Received: August 25, 2023

Revised: December 5, 2023

Published online: January 7, 2024

- [1] C. A. Chatham, T. E. Long, C. B. Williams, *Prog. Polym. Sci.* **2019**, 93, 68.
- [2] BS EN ISO/ASTM 52900:2021, *Additive Manufacturing – General Principles – Fundamentals and Vocabulary*, British Standards Institution **2021**, p. 38.

- [3] I. Campbell, O. Diegel, J. Kowen, N. Mostow, T. Wohlers, I. Fidan, in *Wohlers Report 2022* (Eds: D. Bourell, J. Rensburg van), Wohlers Associates, Washington DC **2022**.
- [4] F. Lupone, E. Padovano, F. Casamento, C. Badini, *Materials* **2022**, 15, 183.
- [5] S. Yuan, F. Shen, C. K. Chua, K. Zhou, *Prog. Polym. Sci.* **2019**, 91, 141.
- [6] R. Goodridge, S. Ziegelmeier, in *Laser Additive Manufacturing - Materials, Design, Technologies and Applications* (Ed: Milan Brandt), Elsevier Inc. **2017**, p. 181, ISBN 9780081004333, <https://doi.org/10.1016/B978-0-08-100433-3.00007-5>.
- [7] Hewlett-Packard Inc., *HP Multi Jet Fusion Technology - A Disruptive 3D Printing Technology for a New Era of Manufacturing - Technical White Paper*, Palo Alto, CA, USA, **2018**.
- [8] C. Fleischmann, R. Donovan, S. R. Woodruff, Y. Feng, *Three-Dimensional (3D) Printing*, **2019**, WO 2019/099031 A1.
- [9] B. Scherer, I. L. Kottenstedde, F. M. Matysik, *Monatshefte Fur Chemie* **2020**, 151, 1203.
- [10] Z. Xu, Y. Wang, D. Wu, K. P. Ananth, J. Bai, *J. Manuf. Process.* **2019**, 47, 419.
- [11] EOS GmbH Electro Optical Systems, *FORMIGA P 110 Velocis*, Krailling, DE **2022**.
- [12] F. Sillani, R. G. Kleijnen, M. Vetterli, M. Schmid, K. Wegener, *Addit. Manuf.* **2019**, 27, 32.
- [13] Hewlett-Packard Inc., *HP Jet Fusion 5200 Series 3D Printing Solutions*, Palo Alto, CA, USA **2019**.
- [14] H. J. O'Connor, A. N. Dickson, D. P. Dowling, *Addit. Manuf.* **2018**, 22, 381.
- [15] T. Palma, M. Munther, P. Damasus, S. Salari, A. Beheshti, K. Davami, *J. Manuf. Process.* **2019**, 40, 76.
- [16] C. S. Abbott, M. Sperry, N. B. Crane, *J. Manuf. Process.* **2021**, 70, 55.
- [17] A. Y. Chen, A. Chen, J. Wright, A. Fitzhugh, A. Hartman, J. Zeng, G. X. Gu, *Adv. Eng. Mater.* **2022**, 24, 2270033.



- [18] K. Chen, Z. H. Koh, K. Q. Le, H. W. B. Teo, H. Zheng, J. Zeng, K. Zhou, H. Du, *Virtual Phys. Prototyp.* **2022**, 17, 631.
- [19] B. Sagbas, B. E. Gümüş, Y. Kahraman, D. P. Dowling, *J. Manuf. Process.* **2021**, 70, 290.
- [20] J. Riedelbauch, D. Rietzel, G. Witt, *Addit. Manuf.* **2019**, 27, 259.
- [21] M. Galati, F. Calignano, S. Defanti, L. Denti, *J. Manuf. Process.* **2020**, 57, 244.
- [22] M. Mele, G. Campana, G. L. Monti, *Addit. Manuf.* **2019**, 30, 100879.
- [23] M. Mele, G. Campana, G. Pisaneschi, G. L. Monti, *Rapid Prototyp. J.* **2020**, 26, 1789.
- [24] H. W. B. Teo, K. Chen, V. T. Tran, H. Du, J. Zeng, K. Zhou, *Polymer* **2021**, 235, 124256.
- [25] S. Rosso, R. Meneghello, L. Biasetto, L. Grigolato, G. Concheri, G. Savio, *Addit. Manuf.* **2020**, 36, 101713.
- [26] C. Cai, W. S. Tey, J. Chen, W. Zhu, X. Liu, T. Liu, L. Zhao, K. Zhou, *J. Mater. Process. Technol.* **2021**, 288, 116882.
- [27] F. Calignano, F. Giuffrida, M. Galati, *J. Manuf. Process.* **2021**, 65, 271.
- [28] G. Craft, J. Nussbaum, N. Crane, J. P. Harmon, *Addit. Manuf.* **2018**, 22, 800.
- [29] H. J. O' Connor, D. P. Dowling, *Addit. Manuf.* **2020**, 31, 100961.
- [30] B. Guo, Z. Xu, X. Luo, J. Bai, *Virtual Phys. Prototyp.* **2021**, 16, S39.
- [31] Sharebot S.r.l., <https://www.sharebot.it/stampanti/snowwhite-2/#technical-details> (accessed: March 2023).
- [32] Hewlett-Packard Inc., *HP MJF Handbook - General Recommendations for Printing Processes*, Palo Alto, CA, USA **2019**.
- [33] M. Mele, G. Campana, G. L. Monti, *Rapid Prototyp. J.* **2021**, 27, 1138.
- [34] R. D. Goodridge, C. J. Tuck, R. J. M. Hague, *Prog. Mater. Sci.* **2012**, 57, 229.
- [35] I. Baesso, D. Karl, A. Spitzer, A. Gurlo, J. Günster, A. Zocca, *Addit. Manuf.* **2021**, 47, 102250.
- [36] N. Hesse, B. Winzer, W. Peukert, J. Schmidt, *Addit. Manuf.* **2021**, 41, 101957.
- [37] C. Yan, L. Hao, L. Xu, Y. Shi, *Compos. Sci. Technol.* **2011**, 71, 1834.
- [38] F.-E. Baumann, N. Wilczok, *Preparation of Precipitated Polyamide Powders of Narrow Particle Size Distribution and Low Porosity*, US 5932689, **1999**.
- [39] H. Scholten, W. Christoph, *Use of a Nylon-12 for Selective Laser Sintering*, US 6245281 B1, **2001**.
- [40] M. Schmid, R. Kleijnen, M. Vetterli, K. Wegener, *Appl. Sci.* **2017**, 7, 462.
- [41] S. Dadbakhsh, L. Verbelen, O. Verkinderen, D. Strobbe, P. Van Puyvelde, J. P. Kruth, *Eur. Polym. J.* **2017**, 92, 250.
- [42] L. Verbelen, S. Dadbakhsh, M. Van Den Eynde, J. P. Kruth, B. Goderis, P. Van Puyvelde, *Eur. Polym. J.* **2016**, 75, 163.
- [43] L. Danilo, *Materiali Polimerici per l'Additive Manufacturing: Caratteristiche Precursori e Prestazioni Meccaniche Dei Prodotti*, Polytechnic of Turin **2018**.
- [44] Hewlett-Packard Inc., *HP 3D High Reusability PA 12 Glass Beads*, Palo Alto, CA, USA, **2019**.
- [45] R. Seltzer, F. M. de la Escalera, J. Segurado, *Mater. Sci. Eng. A* **2011**, 528, 6927.
- [46] A. J. Cano, A. Salazar, J. Rodríguez, *Eng. Fract. Mech.* **2018**, 203, 66.
- [47] S. Arai, S. Tsunoda, A. Yamaguchi, T. Ougizawa, *Addit. Manuf.* **2018**, 21, 683.
- [48] X. Liu, W. S. Tey, J. Y. C. Choo, J. Chen, P. Tan, C. Cai, A. Ong, L. Zhao, K. Zhou, *Addit. Manuf.* **2021**, 46, 102205.
- [49] X. Liu, W. S. Tey, P. Tan, K. K. Leong, J. Chen, Y. Tian, A. Ong, L. Zhao, K. Zhou, *Virtual Phys. Prototyp.* **2022**, 17, 734.
- [50] K. P. M. Lee, C. Pandelidi, M. Kajtaz, *Addit. Manuf.* **2020**, 36, 101533.
- [51] Y. Liu, L. Zhu, L. Zhou, Y. Li, *Rapid Prototyp. J.* **2019**, 25, 1127.
- [52] P. Chen, M. Tang, W. Zhu, L. Yang, S. Wen, C. Yan, Z. Ji, H. Nan, Y. Shi, *Polym. Test.* **2018**, 67, 370.
- [53] G. S. Martynková, A. Slíva, G. Kratošová, K. Č. Barabaszová, S. Študentová, J. Klusák, S. Brožová, T. Dokoupil, S. Holešová, *Polymers* **2021**, 13, 810.
- [54] H. Zarringhalam, N. Hopkinson, N. F. Kamperman, J. J. de Vlieger, *Mater. Sci. Eng. A* **2006**, 435–436, 172.
- [55] P. Chen, H. Wu, W. Zhu, L. Yang, Z. Li, C. Yan, S. Wen, Y. Shi, *Polym. Test.* **2018**, 69, 366.
- [56] C. Schick, *Anal. Bioanal. Chem.* **2009**, 395, 1589.
- [57] S. Greiner, A. Jaksch, S. Cholewa, D. Drummer, *Adv. Ind. Eng. Polym. Res.* **2021**, 4, 251.
- [58] S. Josupeit, L. Ordia, H. J. Schmid, *Addit. Manuf.* **2016**, 12, 189.
- [59] S. Negi, S. Dhiman, R. K. Sharma, *Meas. J. Int. Meas. Confed.* **2015**, 68, 205.
- [60] A. Wörz, K. Wudy, D. Drummer, A. Wegner, G. Witt, *J. Polym. Eng.* **2018**, 38, 573.
- [61] B. Van Hooreweder, D. Moens, R. Boonen, J. P. Kruth, P. Sas, *Polym. Test.* **2013**, 32, 972.
- [62] A. Mokrane, M. Boutaous, S. Xin, *Comptes Rendus - Mec.* **2018**, 346, 1087.
- [63] A. Salazar, A. Rico, J. Rodríguez, J. Segurado Escudero, R. Seltzer, F. Martin De La Escalera Cutillas, *Composites, Part B* **2014**, 59, 285.
- [64] A. Pilipović, T. Brajliah, I. Drstvenšek, *Polymers* **2018**, 10, 1208.